Improved tagged cardiac MRI myocardium strain analysis by leveraging cine segmentation

Mahsa Paknezhad [a,*], Michael S. Brown [b], Stephanie Marchesseau [c]

[a] Department of Computer Science, National University of Singapore (NUS), Singapore
[b] Department of Electrical Engineering and Computer Science, York University, Canada
[c] A*STAR-NUS Clinical Imaging Research Centre, Singapore

ARTICLE INFO

ABSTRACT

Background and objectives: Tagged MR images provide an effective way for regional analysis of the myocardium strain. A reliable myocardium strain analysis requires both correct segmentation and accurate motion tracking of the myocardium during the cardiac cycle. While many algorithms have been proposed for accurate tracking of the myocardium in tagged MR images, little focus has been placed on ensuring correct segmentation of the tagged myocardium during the cardiac cycle. Myocardial strain analysis is usually done by segmenting the myocardium in end-diastole, generating a mesh from the segmentation, propagating the mesh through the cardiac cycle using the output deformation field from motion tracking, and measuring strain on the deforming mesh. Due to the imposed tag strips on the anatomy, identification of the myocardium boundaries is challenging in tagged MR images. As a result, there is no guarantee that the propagated mesh is annotating the myocardium accurately through the cardiac cycle. Moreover, clinical studies indicate that incorrect myocardium annotation can result in overestimation of myocardial strains.

Methods: We introduce a method to improve reliability of strain analysis by proposing a mesh which correctly segments the myocardium in tagged MRI by leveraging the available cine MRI segmentation. In particular, we generate a series of mesh proposals using the cine MRI segmentation and find the propagated mesh proposal which gives the most accurate full-cycle myocardium segmentation.

Results: The mesh selection algorithm was tested on 22 2D MRI scans of diseased and healthy hearts. The proposed algorithm provided more accurate whole-cycle myocardium segmentation compared to the propagated end-diastolic mesh. Regional myocardium strain was measured for 10 3D MRI scans of healthy volunteers using the proposed mesh and the end-diastolic mesh. The measured strain using the proposed mesh was more similar to the expected myocardium strain for a healthy heart than the measured strain using the end-diastolic mesh.

Conclusion: The proposed approach provides accurate whole-cycle tagged myocardium segmentation and more reliable myocardium strain analysis.

© 2019 Elsevier B.V. All rights reserved.

1. Introduction

Myocardium tagging is an imaging technique that allows for the measurement of regional contractile properties of the heart muscles. The degree and extent of regional myocardial dysfunction are important factors in diagnosing cardiomyopathy and ischemic heart diseases [1]. In this imaging modality, parallel dark strips are imposed on the imaging plane by spatial modulation of the mag-netization. The imposed tag strips deform with the underlying myocardium during the cardiac cycle. By tracking deformation of the tag strips on the myocardium through the cardiac cycle, qualitative and quantitative evaluation of intra-myocardial deformation, or so-called strain analysis, is possible. There are two approaches to myocardium strain analysis. In one approach, the myocardium is segmented for a chosen phase (generally end-diastole) in tagged MR images and a mesh is generated from the segmentation. Motion tracking is performed next on the tagged MRI sequence and the resulting deformation field is applied to the generated mesh. Strain is then calculated from the deforming mesh. Point tracking is another way to measure myocardial strain. This approach requires the
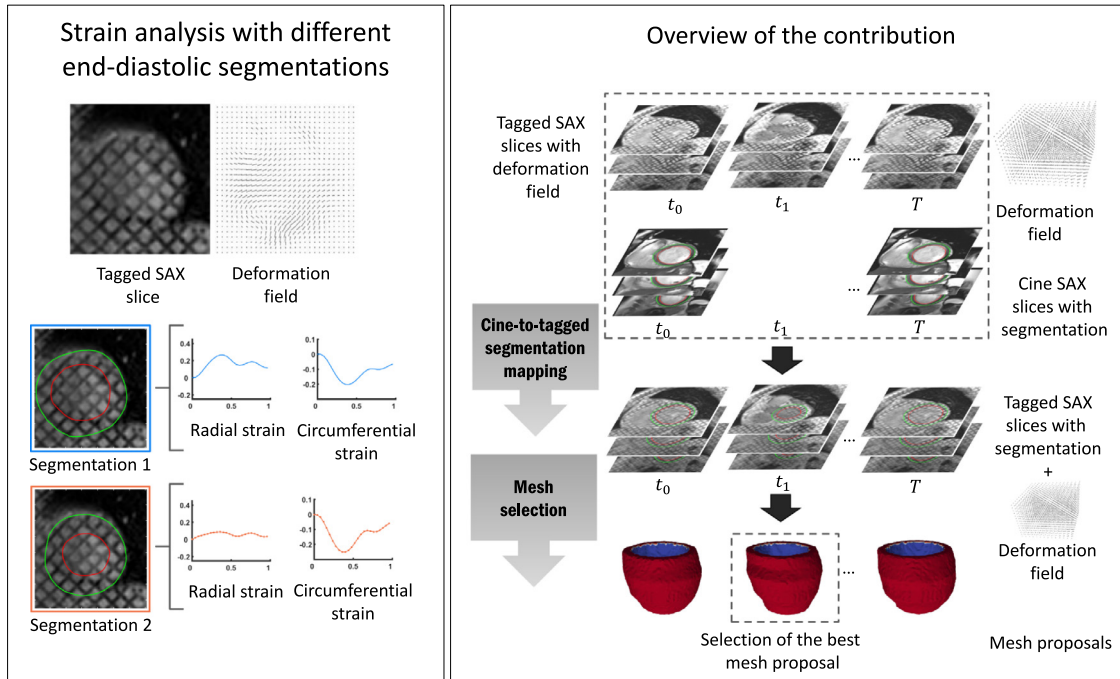
Fig. 1. (Left) Myocardium strain analysis using the segment strain analysis module [2] for a tagged MRI short-axis (SAX) slice conducted with two different end-diastolic segmentations. The measured radial and circumferential strains using each segmentation have different peak values. (Right) An overview of the contributions in this paper. More details are provided in Section 2.

observer to define a few closely located points on the myocardium and tracks these points through the cardiac cycle using the output deformation field from motion tracking. Strain is then measured for the region surrounded by the points. This approach, however, does not provide strain measurement with the desired spatial resolution and across different AHA zones of the left ventricle (LV). Therefore, strain analysis by mesh propagation is more desirable.

A reliable myocardium strain measurement requires accurate myocardium tracking as well as correct segmentation of the myocardium by the deforming mesh. However, structural details, such as myocardial borders are less clear in tagged MR images because of the tag strips. This makes it difficult to identify myocardium boundaries in tagged MR images and to evaluate the deforming mesh with respect to the identified myocardium boundaries. The initial segmentation from which the mesh is constructed and propagated to the other phases is critical on strain analysis, as demonstrated in Fig. 1 (Left), where two different end-diastolic segmentations are used to measure myocardium strain for the tagged short-axis slice shown at the top. The radial and circumferential strain plots for the deforming meshes generated from these two segmentations are also shown. As can be seen, the peak values for the strain plots are different using these two initial segmentations for the same image slice. This inconsistency in strain analysis stems from inaccuracy in full-cycle segmentation of the myocardium by the generated deforming mesh. Our goal is to introduce a method which provides a deforming mesh with accurate myocardium segmentation for the whole cardiac cycle in order to increase reliability of myocardial strain measurements.

Different algorithms have been proposed for segmentation of the myocardium in tagged MR images. Examples include the works by Montillo et al. [3], Milles et al. [4], Qian et al. [5], Histace et al. [6], Garcia-Barnes et al. [7] and Yu et al. [8] in which active contour models and active shape models are trained with complex features to segment the tagged myocardium. These features include tag patterns, edges, ridges, mean and standard deviation of the blood cavity and myocardium, motion information or gradi-

ent vector flow field to segment the tagged myocardium. Denney et al. [9] utilize two level sets for segmentation of the endocardium and epicardium in all the cardiac phases. In the work proposed by Metaxas et al. [10], images are de-tagged using a Gabor filter bank and a deformable model is used to segment the de-tagged images. These algorithms rely on a few specific features which together may not be able to guide segmentation of tagged myocardium accurately during the cardiac cycle. For instance, tag patterns gradually fade during the cardiac cycle. Lack of visible edges in certain MRI scans, and low contrast of some tagged MR images are other problems which prevent these algorithms from being robust solutions to full-cycle tagged MRI segmentation problem.

Apart from the works by Camara et al. [11], Shi et al. [12] and Makram et al. [13], it is often overlooked that standard steady-state free precision (SSFP) cine MR images are also captured along with the tagged MR images. The cine MR images provide a clear view of the endocardium and epicardium and there are validated segmentation algorithms for these sequences. By leveraging the standard cine MR images, one can utilize cine MRI segmentation to generate mesh proposals for tagged MR images and to select the propagated mesh proposal which accurately segments the tagged myocardium. Another advantage of utilizing cine MRI segmentation is that papillary muscles are clearly distinguishable in cine MRI scans and existing segmentation algorithms are able to exclude them from myocardium segmentation. Consequently, utilizing cine segmentations can avoid overestimation of myocardial strains due to inclusion of papillary muscles and trabeculae as reported in the literature [14]. This is while papillary muscles and trabeculae are hardly distinguishable in tagged MR images and are usually included in the segmentation outputs by tagged MRI segmentation algorithms.

Camara et al. [11] rigidly register tagged and cine short-axis slices after de-tagging tagged MR images using steerable pyramid image decomposition. In the work by Shi et al. [12], tagged images are de-tagged using a bandpass filter and an average pseudo-anatomical image is created from the de-tagged image sequence. The corresponding cine images are then registered to the

pseudo-anatomicalimage and their segmentations are propagated to the tagged images. De-tagging methods, however, blur the boundaries in tagged images and consequently decrease the accuracy of the registration algorithms. Makram et al. [13] train a coupled dictionary on patch pairs of cine and tagged MR images and use the trained dictionary for tag removal. The proposed algorithm, however, requires training for different tagging parameters and MRI scanner settings. An algorithm which can robustly identify the tagged myocardium during the cardiac cycle and can propose a deforming mesh with high segmentation accuracy with respect to the identified myocardium is desirable.

2. Contribution

This paper makes two contributions to the tagged MRI myocardium strain analysis problem. These contributions are summarized in Fig. 1 (Right) and described below:

1. Three important features: tag patterns, motion information, and edges are combined such that they can robustly identify the myocardium. Unlike previous methods, this combination is able to identify the myocardium even if the tags are not visible in which case the edges are distinguishable or when the edges are not clear which usually happens when they are modulated by tag patterns. Adding motion information makes identification of the myocardium more robust as will be discussed in the following section. This combination is used by the proposed similarity metric in the next step to map cine MRI segmentation to tagged MRI sequence.

2. A similarity metric is introduced to compare the proposed full-cycle myocardium segmentations for a tagged MRI sequence. The proposed metric evaluates the proposed segmentation with respect to the identified myocardium while giving equal weights to all slices and all phases. Multiple mesh proposals are generated for a tagged MRI sequence by leveraging the mapped cine MRI segmentation. From the generated mesh proposals, deforming meshes are created. The deforming mesh which segments the myocardium more accurately during the cardiac cycle is found by the proposed metric and is used for myocardium strain analysis.

Our experiments suggest that the selected mesh provides more similar strain analysis results to the reported strain curves for healthy hearts when tested on MRI scans of healthy volunteers. Details of the proposed method are provided in the following section.

3. Method

In order to generate mesh proposals for the tagged MRI sequence from cine MRI segmentation, the cine MRI segmentation should be mapped to the tagged MRI sequence. Assuming that the cine and tagged MRI sequence are temporally aligned, a number of challenges arise in mapping cine MRI segmentation to tagged MR images. These challenges include the need to handle existing misalignments among cine short-axis (SAX) slices, among tagged SAX slices, and between tagged and cine MRI sequences while considering size and resolution differences of the two sequences. Therefore, a metric is required for accurate registration of tagged and cine images. The proposed metric should be able to robustly identify the myocardium and its boundaries in the tagged MRI and to register the identified tagged myocardium to the cine myocardium. Fig. 2 gives a summary of how the registration is conducted and how the proposed similarity metric is used to help with the registration and cine-to-tagged segmentation mapping using a myocaridum index map. The A-labeled boxes describe how the myocaridum index map is generated while the B-labeled boxes register the cine and tagged MR images using the myocardium index maps. All these steps together provide a robust algorithm for accurate mapping of cine segmentation to tagged MR images.

The similarity metric is also used to evaluate a proposed deforming mesh for the tagged MRI sequence. We will start by explaining the proposed similarity index. Next, we describe how the cine and tagged MRI sequences are registered and the cine segmentation is mapped on tagged MR images using the proposed metric. We use the mapped cine segmentation to generate a series of mesh proposals and find the mesh proposal which segments the myocardium accurately when propagated through the cardiac cycle.

3.1. The similaity metric

The proposed similarity metric takes advantage of three features from tagged MR images - namely, tag patterns, motion, and edge information to identify the myocardium. Each type of information is extracted in the order which will be presented and adds more details to the results produced from the previous step.

3.1.1. Locating tag patterns

As one of the most important features for differentiating the myocardium from other tissues in tagged MR images, tag patterns are first located in the images through the cardiac cycle by applying a Gabor filter bank. Gabor filter banks have been recognized as an effective tool for myocardium localization in tagged MR images [15]. The bank of Gabor filters is designed considering different frequencies, directions, and tag spacings around the original frequency, direction, and tag spacing settings of the MRI scanner. All filters in the bank are applied to the input image and the filters whose parameters best match the local tag pattern in the image produce higher magnitude responses. By combining parameters of the filters with the highest magnitude responses and applying the resulting filter to the image, an optimal local response can be achieved.

Fig. 2 (A1) shows the result of applying Gabor filter bank to a tagged SAX image with $45°$ and $-45°$ tag strips. The magnitude responses shown on the right have higher values where tag strips appear in the original tagged image. We generated our Gabor filter bank following the works by Chen et. al. [15] and Li et al. [16] and found the magnitude response as an indicator of the existence of tag patterns for all the images and all the slices. The Gabor filter bank was generated with orientation angles $\theta = \theta_{int} + n_1 \times \Delta\theta$ where the initial orientation angles are $\theta_{int} = \pi/4, -\pi/4$ for $45°$ and $-45°$ tag modulations, $n_1 = 0, \pm1, \pm2$, and minimal angular difference of $\Delta\theta = \pi/18$. With tag spacings (S) of 5.27 pixels, the central frequencies were defined by $u = u_0 + n_2 \times u_0$ and $v = v_0 + n_2 \times v_0$ where initial central frequencies are $u_0 = v_0 = 1/S = 0.1897$ and $n_2 = 0, \pm0.1, \pm0.2$. As mentioned before, the myocardium in some images may not have any tag patterns due to tag fading. We handle this issue by combining the location information of tag patterns in other images and motion information as explained in the following paragraph. The following step ensures that our metric is able to localize the myocardium in the images at all the cardiac phases and that the similarity metric does not prioritize one phase over other phases when assessing a proposed full-cycle segmentation.

3.1.2. Combining motion information

In myocardium tagging, tag strips are usually applied over the heart in diastole. The tag strips deform as the myocardium contracts during systole and return to their initial position as the myocardium relaxes. Due to relaxation of the magnetization vectors, the tag strips fade during the cardiac cycle. The fading occurs much faster in the ventricular blood pool because of rapid
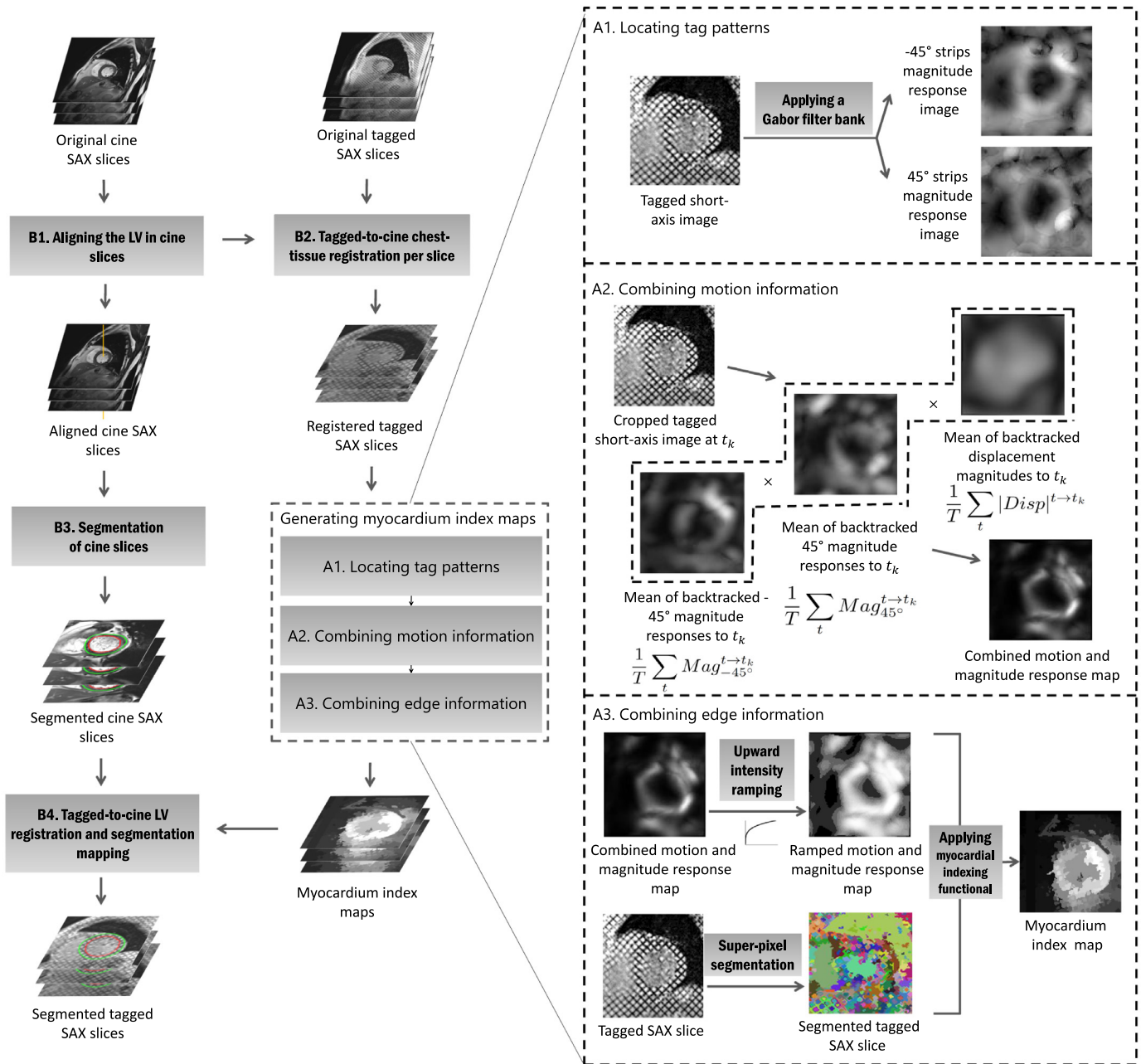
Fig. 2. Steps carried out to register cine and tagged short-axis (SAX) MR images and to map segmentation of cine MR image slices to tagged MR image slices. (A1) Tag patterns are located in all tagged short-axis (SAX) images by applying a Gabor filter bank. The located tag patterns will be used to localize the myocardium in tagged MR images through the cardiac cycle. (A2) Combining motion with tag pattern location information. The combined tag and motion information map identifies the myocardium more clearly compared to the Gabor magnitude response images in step A1. (A3) Combining edge information with the motion and magnitude response map by performing super-pixel segmentation on the original tagged SAX image and applying the myocardium indexing function. (B1) Aligning the cine SAX slices using the method proposed by Fadil et al. [21]. (B2) The soft tissue in the chest walls is used to roughly register the LV in the cine and tagged MR images using the algorithm discussed in Section 3.2.2. (B3) The LV in the cine MR images are segmented using the Segment tool [24] version 2.0 R5454. (B4) The cine segmentations are mapped on the tagged images as described in Section 3.2 using the proposed similarity metric.

motion and mixing of blood in the ventricle, while tag strips fade slower on the myocardium, pericardial fat, liver, and the soft tissue in the chest walls. Areas with large magnitude responses suggest existence of tag strips in those areas in the tagged image. Consequently, large magnitudes can refer to the myocardium as well as other tissues, such as the soft tissue in the chest walls. In order to differentiate the myocardium from other tissues with large magnitude responses, we took advantage of the fact that the myocardium moves while other tissue types hardly move during the cardiac cycle. We combined the acquired displacement field from tagged MRI sequence with the magnitude responses using the obtained displacement field from motion tracking of the heart in tagged MR images [7].

Using the resulting displacement field, we registered all the magnitude images in the cardiac cycle to each phase and found the mean magnitude image for each phase. More specifically, let us define the magnitude responses for 45° and -45° tag strips as $\{Mag_{45°}^t\}_{t=1}^T$ and $\{Mag_{-45°}^t\}_{t=1}^T$ for a cardiac cycle with T cardiac phases and the registered magnitude responses to time t_k as $\{Mag_{45°}^{t \to t_k}\}_{t=1}^T$ and $\{Mag_{-45°}^{t \to t_k}\}_{t=1}^T$, respectively. Let us also define the

obtained displacement field from time t in the cardiac cycle to the end-diastolic phase as $\{Disp^t\}_{t=1}^T$ and the backtracked displacement magnitude from time t to time t_k as $\{|Disp|^{t \to t_k}\}_{t=1}^T$. Then, the combined motion information and magnitude response (M^{t_k}) for time t_k is calculated as follows:

$$M^{t_k} = \left(\frac{1}{T} \sum_t Mag_{45°}^{t \to t_k} \right) \times \left(\frac{1}{T} \sum_t Mag_{-45°}^{t \to t_k} \right) \times \left(\frac{1}{T} \sum_t |Disp|^{t \to t_k} \right)$$

(1)

where $\times$ is pixel-wise multiplication of the resulting three mean images: $\frac{1}{T} \sum_t Mag_{45°}^{t \to t_k}$, $\frac{1}{T} \sum_t Mag_{-45°}^{t \to t_k}$, and $\frac{1}{T} \sum_t |Disp|^{t \to t_k}$. Fig. 2 (A2) shows an example of combining motion and magnitude responses for a tagged SAX image. The first two images from the bottom left to the top right show the mean of the registered Gabor magnitude responses to time t_k for $-45°$ and $45°$ tag strips, respectively. The last image is the mean of the backtracked displacement magnitudes to time t_k. As the output image suggests, this task differentiates the myocardium from other tissues more effectively compared to the resulting magnitude responses in the tag pattern localization step (Fig. 2 [A1]). The colored regions in the 'Segmented tagged SAX slice' represent different identified super-pixels and the bright super-pixels in 'Myocardium index map' show high probability of locating LV muscles in those super-pixels.

3.1.3. Combining edge information

The combined motion and magnitude response outputs a blurred image with no clear edge information. In order to add any existing myocardium boundary information to the combined motion and magnitude response map, we extract the edge information from the original tagged MR images. Extracting the edges from the tagged MR images is performed using a super-pixel segmentation algorithm [19] with high sensitivity to small intensity differences and weak edges. The super-pixels outputted by the super-pixel segmentation algorithm divide the original tagged MR image into regions with similar intensity values that are separated by the identified edges in the image. Having extracted these super-pixels, we utilize the combined motion and magnitude response map to measure the probability of myocardium being in each super-pixel and assign a high contrast value to the super-pixels for which a high probability is measured. This task is carried out using the salient object detection algorithm proposed by Cheng et al. [20] where the global contrast of each super-pixel is measured with respect to all the other super-pixels in the image. Contrast for each super-pixel r_k is measured using the intensity histogram in that super-pixel and those of all the other super-pixels while giving more weight to the neighboring regions and less weight to distant regions following the function below:

$$MI(r_k) = \alpha(r_k) \sum_{r_k \neq r_l} exp[-D_s(r_k, r_l)/\sigma_s^2] \times \beta(r_l) \, M_{r_k} \log(D_m(r_k, r_l))$$

(2)

The intensity histogram is measured from the combined motion and magnitude response map for each super-pixel. We call the final contrast map measured for the combined motion and response map using this function as myocardium index (MI) map since super-pixels with higher contrasts specify regions that have a higher probability of containing myocardium. $D_m(r_k, r_l)$ is a distance metric between the two super-pixels r_k and r_l in the image. If the combined motion and magnitude response map is considered as a grayscale image, the distance metric is measured as $D_m(r_k, r_l) = \sum_{i=1}^{n_k} \sum_{j=1}^{n_l} \left[p(I_{k,i}) p(I_{l,j}) D(I_{k,i}, I_{l,j}) \right]$ where $p(I_{k,i})$ is the probability of the ith intensity $I_{k,i}$ in the probability density function of super-pixel r_k with n_k different intensity values and $D(I_{k,i}, I_{l,j})$ denotes distance between intensity $I_{k,i}$ and intensity $I_{l,j}$. M_{r_k} is the weighted average intensity for super-pixel r_k using the probability density function for super-pixel r_k.

To favor super-pixels with higher average combined motion and magnitude response compared to their surrounding super-pixels, the spatial weighting term $exp[-D_s(r_k, r_l)/\sigma_s^2]$ increases the effect of spatially closer super-pixels. $D_s(r_k, r_l)$ is the spatial distance between super-pixel r_k and r_l and is measured as the Euclidean distance between their centroids. Parameter σ_s limits the effect of spatial distance weighting. The value of σ_s^2 was set to 0.4 with pixel coordinates normalized to [0,1]. $\beta(r_l)$ is the number of pixels in super-pixel r_l to emphasize contrast to bigger super-pixels. A center bias $\alpha(r_k) = \exp(-7d_k^2)$ is imposed to favor super-pixels that are spatially closer to the center coordinates of the LV, where d_k is the average distance between pixels in region r_k and the LV center. In this way, moving super-pixels with tag patterns and closer to the center of the LV are given higher myocardium index values.

The contrast of the combined motion and magnitude response map is enhanced by passing it through an upward intensity ramping filter with a fixed gamma value of 0.25 before feeding it to the myocardium indexing function (see Fig. 2 [A3]). The main goal is to decrease the measured contrast $D_m(r_k, r_l)$ between regions with high average value for motion and magnitude response and therefore to assign similar myocardium index values to these super-pixels.

The myocardium indexing function was applied on the motion and magnitude response images and the original tagged images for all the slices and all phases to generate the myocardium index maps. Due to high sensitivity of the super-pixel segmentation algorithm to intensity differences and weak edges and existence of noise in the image, the segmentation output is made up of very small super-pixels. The myocardial indexing function highlights the super-pixels which belong to the myocardium. Fig. 2 (A3) shows the result of applying a super-pixel segmentation algorithm on a tagged SAX image acquired on a Siemens Trio scanner. The parameters for the super-pixel segmentation algorithm and the myocardium indexing function were tuned to ensure a segmentation with sufficient sensitivity and myocardium contrast.

Finally, the proposed similarity metric measures two parameters on the resulting myocardium index maps: the first parameter measures the gradient of the area enclosed by the proposed segmentation from the surrounding area, which is found by sampling intensities on the perpendicular lines to the endocardium and epicardium annotations. The second parameter adjusts the center of the segmentation on the blood pool by finding the location with the highest centricity for the corresponding segmentation. The similarity metric is formulated as follows:

$$E(seg) = \sum_{slices} \sum_{phases} E_{gradient}(seg) + \sum_{slices} \sum_{phases} E_{centricity}(seg)$$

(3)

Let endocardium segmentation be denoted by the n 2D points in the set $X = (X_1, X_2, \ldots, X_n)$ and the epicardium segmentation be defined by the n 2D points in the set $Y = (Y_1, Y_2, \ldots, Y_n)$. If the orthogonal vector to the endocardium annotation at point X_i is defined as dX_i and the orthogonal vector to the epicardium annotation at point Y_i is defined as dY_i, then the gradient energy is defined as:

$$E_{gradient}(seg) = \sum_{i \in \{1,n\}} \sum_k (X_i + k \times dX_i) - (X_i - k \times dX_i)$$
$$+ \sum_{i \in \{1,n\}} \sum_k (Y_i - k \times dY_i) - (Y_i + k \times dY_i),$$

(4)

where k is the number of sampled points on the orthogonal vectors. The centricity energy is measured using the following function where the mean radius of the endocardium (epicardium) segmentation for each slice is denoted as avg_{endo} (avg_{epi}) and $circle_r$

refers to a circle at the center of the segmentation with radius r, then :

$$E_{centricity} = A_{avg_{epi}} - A_{avg_{endo}}, \tag{5}$$

where

$$A_r = \sum_{p \, \in \, circle_r} \mathrm{MI}(p), \tag{6}$$

and p is a pixel coordinate in the myocardium index map.

3.2. Cine-to-tagged segmentation mapping

Although both cine and tagged MR images are acquired from the same SAX planes, there are different types of spatial misalignment in these two sequences due to patient repositioning as well as inconsistencies in breath-hold position. More specifically, (1) the cine and tagged image sequences are generally not aligned, (2) the cine SAX slices are not aligned with respect to each other, and (3) the tagged SAX slices are not aligned with respect to each other. We handle these spatial misalignments following the three steps described below:

3.2.1. Long-axis alignment of cine SAX slices

In the first place, the LV in cine SAX slices is aligned using the algorithm proposed by Fadil et al. [21]. In this algorithm, the LV is automatically located in each cine SAX slice and the slices are aligned using the LV location information. Another approach to align cine SAX slices is the method proposed by Villard et al. [22] in which the long-axis view of the heart is utilized to align the slices. Having aligned the cine slices, a cine segmentation algorithm is applied to the cine SAX slices. While any segmentation algorithm can be used at this stage, we took advantage of the automatic segmentation algorithm proposed by Tufvesson et al. [23] which is implemented in the Segment tool [24] version 2.0 R5454. This segmentation will be mapped to the tagged MR images as will be explained in Section 3.2.3.

3.2.2. Chest-tissue-registration of tagged and cine images

In this step, we target the misalignment between tagged and cine SAX slices which occurs due to patient repositioning. The tag patterns on tagged images make common registration algorithms for medical images, such as the well-known Demons algorithm [25] or mutual-information-based registration algorithms [26] ineffective to register tagged and cine images. Consequently, a different strategy is required to register these two sequences. The soft tissue in the chest walls is a useful guide for registering tagged and cine images as it hardly deforms in subsequent MRI acquisitions. We adopted a multi-scale low-rank matrix decomposition method proposed by Peng et al. [27] for registering tagged and cine SAX slices while taking advantage of constant visibility of the soft tissue in the chest walls. The main advantage of this method is its ability to handle corruptions, small additive noise, and large occlusions in the input images; in our case the tagged strips in tagged MR images.

This technique requires a batch of images which are considered as the columns of a matrix. A set of transformations is found, one for each image, to minimize the rank of the matrix. In order to prepare a batch of images to register a tagged SAX MR image to its corresponding cine SAX MR image, the cine SAX images around each time point t_k in time are registered to the cine SAX image at time t_k using b-spline registration [28] in order to remove any complex deformations. These cine images (fixed images) together with the tagged SAX image at time t_k (moving image) are considered as the batch of images that are registered using low-rank decomposition. An image matrix is made from the uncropped cine and tagged images that contain the soft tissue in the chest walls

through the cardiac cycle which provide structure and guide the transformation in order to achieve suitable registration results. Our algorithm is defined to transform and register the tagged SAX image to all the other cine SAX images in the matrix iteratively while keeping the cine images intact. This task is carried out to register tagged SAX image for a randomly selected phase to its corresponding cine SAX image and the resulting transformation is applied to all the images in the tagged SAX slice.

Registration of the soft tissue in the chest walls does not guarantee that the tagged and the cine LV will also be well-registered. That is mainly due to inconsistencies in breath-hold position while acquiring tagged and cine images which refers to the difference in the amount of air that is held in the lungs while the images are acquired. This problem is handled in the next step.

3.2.3. Tagged-to-cine LV registration and segmentation mapping

The previous steps roughly align the LV in the cine and tagged MRI sequence and allow us to crop a region around the LV in the tagged MRI slices using the same bounding box used for the cine MRI sequence. In the next step, a brute-force search is carried out in this cropped region on each tagged SAX slice by sliding the corresponding cine segmentation around and finding the location which maximizes the similarity metric described in Section 3.1. Having found the best location, the tagged SAX slice was adjusted such that the cine segmentation falls on the located optimal position. After registering the tagged SAX slices to their corresponding cine SAX slices in this way, the cine segmentation is mapped to the tagged slices.

The previous steps register tagged and cine SAX slices and provide full-cycle segmentation for tagged SAX images using the introduced similarity metric. The similarity metric is next used to select the deforming mesh with the most accurate full-cycle myocardium segmentation from a series of deforming mesh proposals. As mentioned before, accurate segmentation is necessary for a reliable regional strain analysis of the myocardium.

3.3. Improved myocardium strain analysis

Regional strain analysis allows for qualitative and quantitative evaluation of intra-myocardial deformation and is an effective metric for diagnosing ischemic heart disease. This analysis is usually performed by (1) segmentation of the myocardium in tagged MR images for one specific cardiac phase, (2) registration of the tagged MR images in that phase to the images in the other phases, and (3) propagating the mesh generated from the segmentation to the other phases using the resulting displacement field from the registration. A reliable myocardium strain analysis requires both correct myocardium tracking as well as accurate annotation of the myocardium boundaries during the cardiac cycle. However, the aforementioned strategy to measure the strain makes accuracy of myocardium segmentation highly dependent on the initial mesh chosen to propagate to the other phases.

The end-diastolic mesh is generally the chosen mesh to propagate to the other phases for strain analysis. While many algorithms have been proposed and evaluated for motion tracking in tagged MRI sequences, such as the TDFFD registration algorithm [17], there has been no means to evaluate the deforming mesh in terms of accuracy in tagged myocardium segmentation. As a result, there is no guarantee that the propagated mesh is annotating the myocardium correctly during the cardiac cycle. Having a full-cycle segmentation for the tagged MRI sequence using the cine-to-tagged segmentation mapping algorithm and a similarity metric to evaluate a proposed segmentation, a more accurate deforming mesh in terms of segmenting the myocardium can be proposed. This aim is achieved by generating a mesh for each cardiac-phase segmentation and propagating this mesh to the other phases

Table 1

Values assigned to the parameters for each algorithm for our dataset and the cMac challenge 2011 dataset [18]. The parameter values were either set to the values advised in referred publications or tuned by applying the algorithm on randomly chosen images from the dataset.

Algorithm	Parameter	Our dataset	cMac dataset
Gabor filter bank	θ_{int}	$\pi/4, -\pi/4$	$0, \pi/2$
	$\Delta\theta$	$\pi/18$	$\pi/18$
TDFFD registration	control points	5	4
	number of samples	10,000	10,000
	λ	0.1	0.1
Super-pixel segmentation	σ for Gaussian filter	0.2	2
	intensity threshold	30	0
	min component size	5	5
Upward intensity ramping	γ	0.25	0.25
Myocardium indexing	σ_s^2	0.4	0.4
similarity metric	k	$\{0,\ldots,5\} \times Reso.$	$\{0,\ldots,5\} \times Reso.$
Brute force search	box size	60×60 pixels	60×60 pixels
	spatial interval	3 pixels	3 pixels

using the acquired displacement field from tagged MRI sequence. The mesh proposal which provides the most accurate myocardium segmentation is then selected by measuring and comparing the similarity metric for all the propagated mesh proposals. Assuming there are T mesh proposals for strain analysis, where T is the number of phases within each cardiac cycle, the best propagated mesh is defined as the one for which the measured similarity (Eq. 3) is maximized.

In the next section, we will evaluate our proposed method using our own dataset and the available dataset from the cardiac motion analysis challenge 2011.

4. Validation

In order to evaluate the proposed method, we measured the accuracy of the proposed myocardium segmentation for the selected deforming mesh versus the deforming end-diastolic mesh in Sections 4.1 and 4.2, respectively. Section 4.3 analyses the results of strain analysis using the selected deforming mesh for 10 healthy subjects from the cMac dataset.

4.1. Cine-to-tagged-segmentation mapping accuracy

We applied our cine-to-tagged segmentation mapping algorithm on 12 MRI scans of patients with degenerative mitral valve regurgitation (DMR) and 10 MRI scans of healthy subjects. Both the DMR and healthy cases were scanned in 2D by a 3T Siemens Trio scanner in 11−20 heartbeats per slice. A series of 10−14 SSFP cine and tagged SAX slices were acquired for each case with 8 mm slice thickness and slice spacing of 9.6 mm. All sequences comprised 25 cardiac phases with spatial resolutions in the range of 1.17−1.77 mm for cine and 1.33−2.56 mm for tagged images. All tagged MR images went through 45° and −45° modulation with 8 mm tag spacing. The tagged MRI sequences covered the whole cardiac cycle and were temporally aligned to their corresponding cine MRI sequence. Steps (A1), (B2), and (B4) in Fig. 2 were implemented in Matlab programming language, while steps (A2), (A3), and (B1) were implemented in C++ programming language. Step (B3) was performed using the Segment tool [24] and the C++ implementation of the TDFFD registration algorithm [17] was utilized. Four different scales were defined for the chest-tissue-registration algorithm with a maximum of 30 iterations for each scale and a relative change threshold of $1e-5$. Motion tracking was performed using the TDFFD registration algorithm backwards in the cardiac cycle with a resolution of 5 control points in each dimension for the b-spline velocity grid, 10000 samples, and λ weight of 0.1. The threshold value, the σ for the Gaussian filter, and the minimum component size were set to 30, 0.2, and 5, respectively, for the

Table 2

Error measurement for the mapped cine MRI segmentation by the cine-to-tagged segmentation mapping algorithm compared to the reference manual segmentation. Error measurements are carried out on the dataset ($n = 22$) for the final frame (FF) and the end-systolic (ES) phase using dice similarity coefficient (DSC) and point-to-curve distance (P2C).

(FF & ES)	DSC	P2C (mm)
Endocardium basal	0.88 ± 0.04	1.88 ± 0.57
Endocardium mid-ventricular	0.83 ± 0.08	2.23 ± 0.85
Endocardium apical	0.75 ± 0.10	2.34 ± 0.85
Epicardium basal	0.95 ± 0.03	1.28 ± 0.64
Epicardium mid-ventricular	0.93 ± 0.05	1.64 ± 0.94
Epicardium apical	0.91 ± 0.05	1.76 ± 1.01

Differences are expressed as mean $\pm$ std. A perfect match with the manual reference would give a DSC value equal to 1 and a P2C value equal to 0. FF = final frame, ES = end-systole.

super-pixel segmentation algorithm. The spatial distance limiting sigma σ_s was set to 0.4 for the myocardium indexing function. An upward intensity ramping function with $\gamma = 0.25$ was generated and applied on the combined motion and magnitude response map before applying the myocardium indexing function. A range of $\{0,\ldots,5\} \times$ Resolution was defined for the k in the gradient energy function (Eq. (4)). Brute-force search was carried out for segmentation mapping in a 60×60 pixels window with a step-size of 3 pixels.

In both our dataset and the cMac dataset that we will work on later, the tagged MRI sequences covered the whole cardiac cycle whereas the number of time frames within the cardiac cycle could be different. When a difference in the number of time frames in the tagged and cine MRI sequences were detected, the tagged MRI sequence was down- or up-sampled using the segment tool [24] to match the number of time frames in the corresponding cine MRI sequence. Temporal alignment between the cine and tagged MRI sequences was assumed in the proposed algorithm. In case of temporal misalignment, the meta-tag describing the trigger time for acquisition of the corresponding frame can be found in the Dicom header and can be used to temporally align the two sequences similar to the work by Shi et al. [12].In case the tagged MRI sequence does not cover the whole cardiac cycle, only the cine MRI frames that are acquired in the same partial cardiac cycle as the tagged MRI sequence will be considered for segmentation mapping and the rest of the pipeline stays intact.

Table 1 summarizes these parameter values for this dataset (third column). We will explain in the last paragraph in Section 4.3 how these values were selected. Table 2 shows the accuracy of the segmentation mapping algorithm compared to
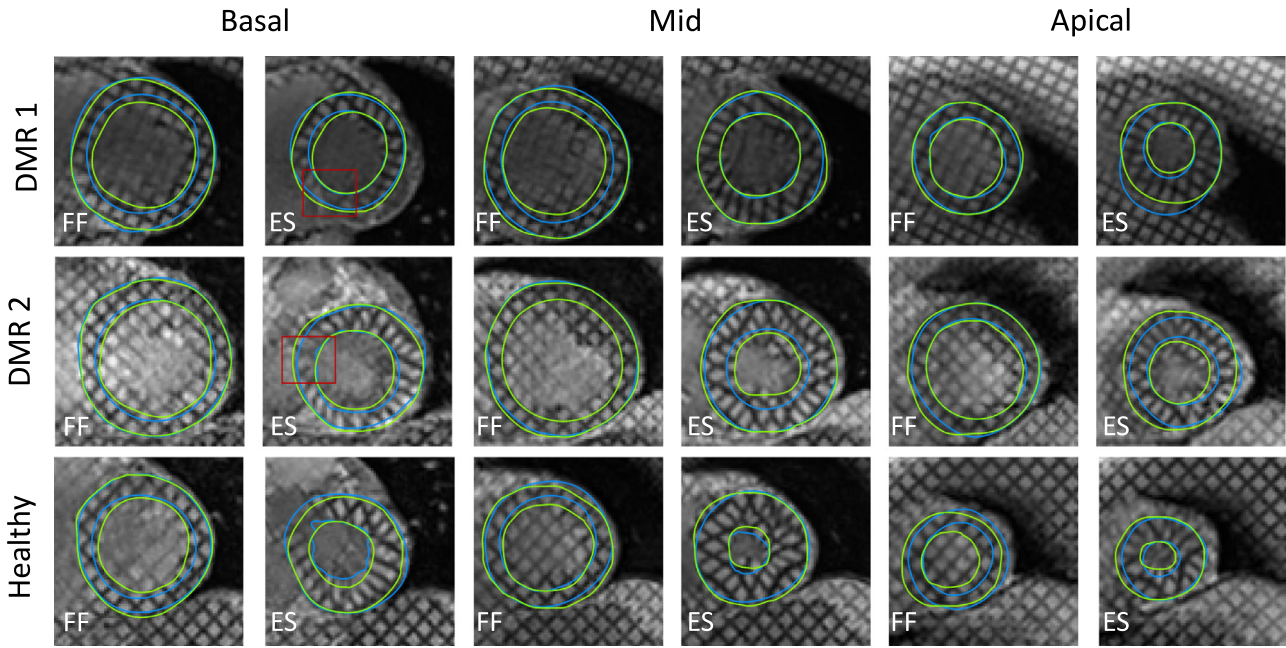
Fig. 3. Three examples of cine-to-tagged MR image segmentation mapping (blue) for two patients with degenerative mitral valve regurgitation (DMR), and a healthy case (Healthy) at the final frame (FF) and the end-systole (ES). Also shown is the manual segmentation (green) for these cases. One can see that cine-to-tagged segmentation mapping is a good strategy to handle tag fading and poor visibility of myocardial borders (red boxes). (For interpretation of the references to colour in this figure legend, the reader is referred to the web version of this article.)

manually segmented tagged MR images by an expert for the final frame (FF) and the end-systolic (ES) phase using the dice similarity coefficient (DSC) [29] and point-to-curve distance (P2C) [30]. The measured DSC values for all slice sections and for both endocardium and epicardium were higher than 0.80 except for the apical endocardium segmentations, and the P2C error measurements were less than 2 mm except for the mid-ventricular and apical endocardium. The mean P2C measurement for all slice sections and for both endocardium and epicardium is less than 2.34 mm. Fig. 3 shows three examples of cine-to-tagged segmentation mapping (blue) and the manual segmentation (green) for two DMR cases and one healthy case. It is important to mention that as our later measurements of intra-observer variability in manual segmentation of tagged MR images in Section 4.2 imply, the experts are not confident in their manual segmentation and often guessing is involved in the segmentation process for tagged MR images. Therefore, many readers may disagree with the manual segmentations (green line) in Fig. 3. However, one can say that a close correspondence can be seen between the mapped cine and manual segmentations and the mapped cine segmentations are seen to be fairly well-aligned on the tagged heart during the cardiac cycle despite tag fading and poor visibility of myocardial borders (see red boxes). This justifies our opinion that mapping myocardium segmentation from cine MRI sequences in which myocardium is clearly visible is a more reliable strategy for annotating the LV in tagged MRI sequences since it reduces the guessing factor from the tagged MR image segmentation.

4.2. Myocardium segmentation accuracy for the proposed mesh vs. end-diastolic mesh

We used the same dataset to evaluate accuracy of myocardium segmentation for the selected deforming mesh by our algorithm. The TDFFD algorithm was used for motion tracking similar to the analysis on segmentation mapping accuracy. The mesh proposals were propagated using the resulting displacement field from motion tracking. The best deforming mesh was selected by the

proposed algorithm and myocardium segmentation was evaluated for the selected deforming mesh and the deforming end-diastolic mesh. Fig. 4 shows examples of the segmentation by the selected deforming mesh compared to the segmentation by the deforming end-diastolic mesh for both DMR and healthy cases. For case DMR1, for instance, the endocardium for the proposed mesh is close to the blood pool. As a result, there is no missing muscle thickness even at end-systole when the tags are blurred compared to the segmentation by the end-diastolic (red) mesh.

Tables 3 and 4 compare accuracy of endocardium and epicardium segmentation by the proposed mesh with manually segmented tagged MR images by an expert for the FF and ES phase using DSC and P2C distance. Also shown is the intra-observer variability (difference between manual segmentation performed twice) as the best possible accuracy. The tables indicate that for both endocardium and epicardium, the segmentation by the selected deforming mesh is more similar to the manual segmentation compared to the segmentation by the deforming end-diastolic mesh. For basal endocardium, for example, the myocardium segmentation error measurements for the selected deforming mesh are DSC $= 0.86 \pm 0.04$ and P2C $= 2.17 \pm 0.71$ mm, whereas these measurements for the end-diastolic mesh are DSC $= 0.81 \pm 0.06$ ($p < 0.001$) and P2C $= 2.80 \pm 1.00$ mm ($p < 0.01$). The errors between the second observer segmentation and the reference manual segmentation are DSC $= 0.91 \pm 0.02$ and P2C $= 1.38 \pm 0.30$ mm for the basal endocardium, which are not significantly different from the errors for the selected deforming mesh. Once cine segmentation, Gabor filter magnitude responses and the deformation field from myocardium tracking are provided, the algorithm takes approximately 13 min when executed on a personal computer with i7 2600 CPU @ 3.40 GHZ and 8GB RAM for a MRI scan with 13 cine and tagged SAX slices and 25 cardiac phases.

4.3. Regional strain analysis on cMac dataset

In order to analyze the performance of our method on strain analysis results, we tested our mesh selection algorithm on
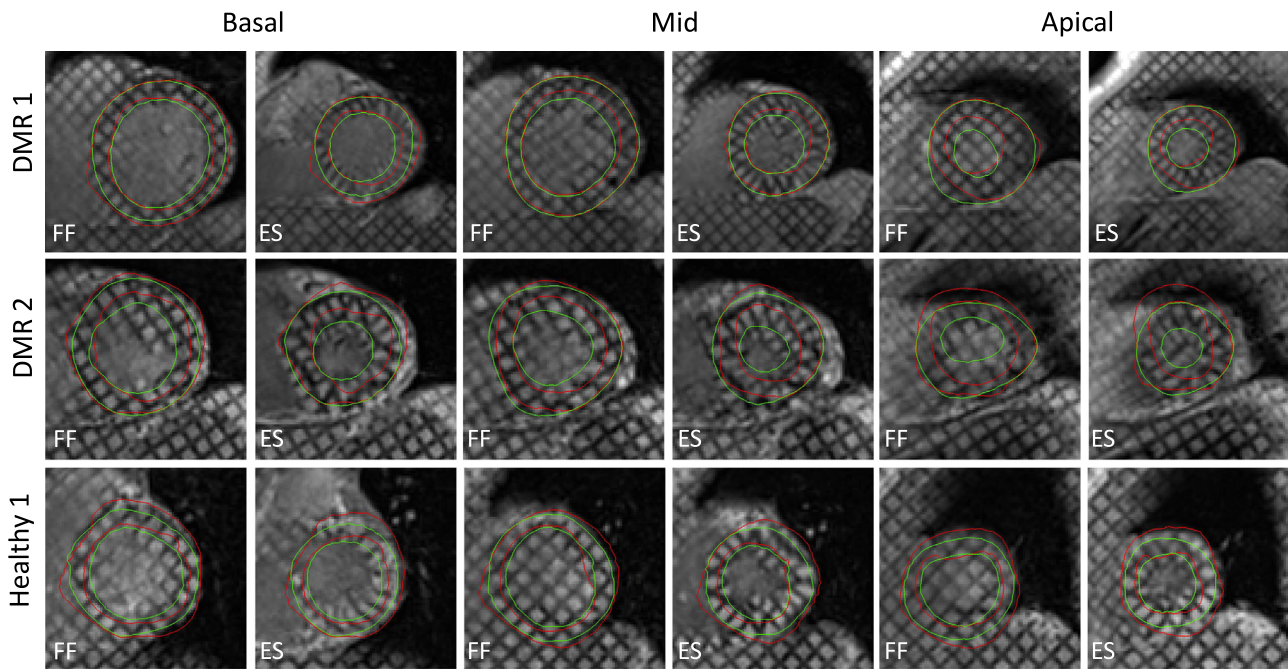
Fig. 4. Three examples of myocardium segmentation for the selected deforming mesh by our algorithm (green) for two cases with degenerative mitral valve regurgitation (DMR 1, 2) and one healthy case (Healthy 1) at the final frame (FF) and the end-systole (ES). Also shown is the myocardium segmentation by the deforming end-diastolic mesh (red) which is commonly used for strain analysis. (For interpretation of the references to colour in this figure legend, the reader is referred to the web version of this article.)

Table 3

Myocardium segmentation error measurement for the selected deforming mesh (second column) and the deforming end-diastolic mesh (third column) compared to the intra-observer variability (fourth column). Error measurements are carried out against manual segmentation (ground truth segmentation) on the dataset ($n = 22$) for the final frame (FF) and the end-systolic (ES) phase as dice similarity coefficient (DSC).

Dice similarity coefficient	Proposed mesh	End-diastolic mesh	Intra-observer variability
Endocardium basal***	**0.86 ± 0.04**	0.81 ± 0.06	0.91 ± 0.02
Endocardium mid-ventricular***	**0.81 ± 0.08**	0.76 ± 0.10	0.86 ± 0.06
Endocardium apical**	**0.71 ± 0.12**	0.63 ± 0.14	0.78 ± 0.11
Epicardium basal**	**0.92 ± 0.02**	0.91 ± 0.03	0.95 ± 0.01
Epicardium mid-ventricular***	**0.92 ± 0.04**	0.89 ± 0.05	0.95 ± 0.02
Epicardium apical*	**0.89 ± 0.06**	0.85 ± 0.08	0.92 ± 0.03

*, **, and *** indicate that myocardium segmentation for the selected deforming mesh is significantly better than myocardium segmentation for the deforming end-diastolic mesh with p-values less than 0.05, 0.01, and 0.001, respectively.

Table 4

Comparison between myocardium segmentation for the selected deforming mesh (second column) and the deforming end-diastolic mesh (third column) compared to the intra-observer variability (fourth column). Error measurements are carried out against manual segmentation (ground truth segmentation) on the dataset ($n = 22$) using point-to-curve distance (P2C) for the final frame (FF) and the end-systolic (ES) phase.

Point to curve distance	Proposed mesh	End-diastolic mesh	Intra-observer variability
Endocardium basal**	**2.17 ± 0.71 mm**	2.80 ± 1.00 mm	1.38 ± 0.30 mm
Endocardium mid-ventricular*	**2.41 ± 0.90 mm**	2.88 ± 1.11 mm	1.86 ± 0.70 mm
Endocardium apical**	**2.57 ± 1.04 mm**	3.44 ± 1.40 mm	1.91 ± 0.73 mm
Epicardium basal*	**1.89 ± 0.54 mm**	2.10 ± 0.76 mm	1.18 ± 0.23 mm
Epicardium mid-ventricular**	**1.97 ± 0.84 mm**	2.43 ± 1.19 mm	1.19 ± 0.30 mm
Epicardium apical*	**2.06 ± 1.03 mm**	2.69 ± 1.25 mm	1.43 ± 0.41 mm

* and ** indicate that myocardium segmentation for the selected deforming mesh is significantly better than the myocardium segmentation by the deforming end-diastolic mesh with p-values less than 0.05 and 0.01, respectively.

10 randomly selected healthy volunteers from the cMac 2011 dataset. The dataset consists of 3D tagged MRI scans of healthy volunteers together with their corresponding 2D cine SSFP MRI sequence acquired using a 3T Philips Achieva System. All cine images were acquired during breath-holds of approximately 15 s and were gated to the vector ECG. The 3D tagged MRI sequences were ob-tained in three sequential breath-holds acquisitions in each orthog-onal direction. The tag distance was set to 7 mm with flip angle $= 19 - 25°$. Spatial resolution of the tagged images is 0.96 mm and their temporal resolution is in the range of $21-38$ cardiac phases. The cine scans consist of images with spatial resolution of $1.15-1.25$ mm and all the sequences comprise 30 cardiac phases. The
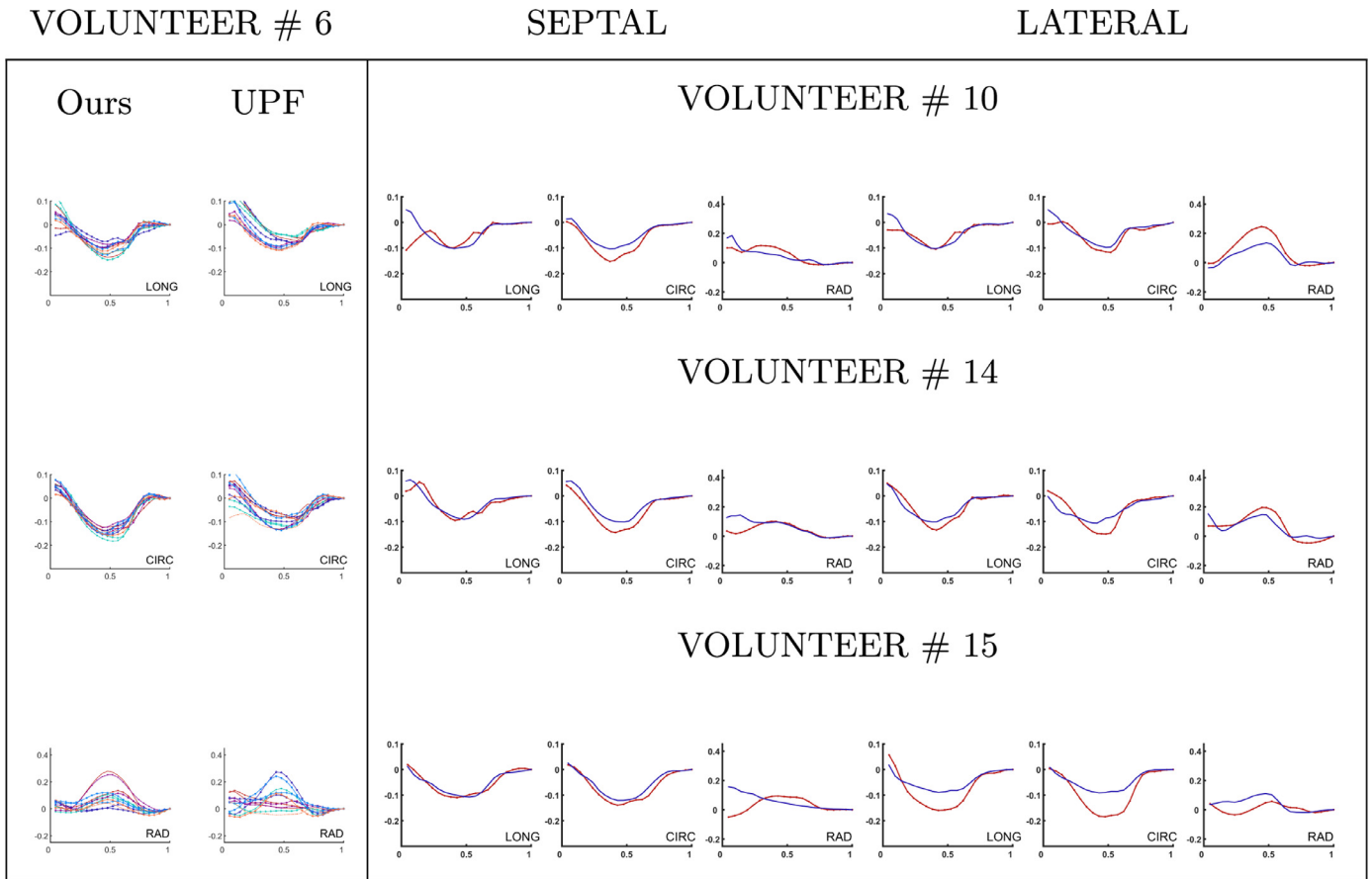
Fig. 5. (Left) Longitudinal (LONG), circumferential (CIRC), and radial (RAD) strain curves for volunteer V6 for our selected deforming mesh plotted as a function of time (normalized by one heart period) and the same plots for the UPF challenger in cMAC 2011. The curves show the average strain across 12 AHA zones (corresponding to basal and mid-ventricular regions). (Right) Strain plots for septal and lateral sections of the left ventricle for the UPF challenger (blue line) and the proposed deforming mesh (red line) plotted as a function of time (normalized by one heart period) for volunteers V10, V14, and V15. The strain curves are not post-processed or smoothed. (For interpretation of the references to colour in this figure legend, the reader is referred to the web version of this article.)

cine MRI sequences were down- or up-sampled using the segment tool [24] to match the temporal resolution of their corresponding tagged MRI series and was segmented using the segment tool [24]. To register the cine segmentation to the 3D tagged MRI sequence, the corresponding tagged image planes from the 3D tagged MRI sequence were extracted and used to map the cine segmentation to the tagged images using the proposed algorithm. After the cine segmentations were successfully mapped to the tagged MRI slices, these segmentations were used to generate 3D mesh proposals. T mesh proposals were generated where T is the total number of cardiac phases for the subject. Motion tracking was performed on the 3D tagged MRI sequence and the measured displacement field was applied to the generate mesh proposals to give us 3D moving meshes. similarity was measured for the deforming meshes on the tagged SAX MRI sequences which were sliced out by the corresponding cine SAX slices and the best deforming mesh proposal was selected.

Finally, 3D strain analysis including longitudinal, radial and circumferential strain analysis was performed using the selected deforming mesh on the 3D tagged MRI sequence. We compared our strain analysis results with those of the UPF challenger in cMac 2011 [18]. The TDFFD registration algorithm was used for both cases, while the mesh to propagate was different. The UPF challenger uses a left ventricular model which is deformed manually to match the manual segmentation of the end-diastolic phase in cine SAX slices. Fig. 5 (Left) shows the strain curves averaged across 12 AHA zones (corresponding to basal and mid-ventricular

regions) as a function of time for our proposed deforming mesh and the UPF challenger's results for volunteer V6. Our strain curves show more similar peak values to the reported measurements by Moore et al. [31] for healthy volunteers. According to their measurements on healthy hearts, the peak values for the strain curves should reach up to 45% for radial strain, −20% for circumferential strain, and −16% for longitudinal strain. Our strain curves also converge better to zero at the final frame, and all regions contract more synchronously compared to the UPF challenger's results using the deformed LV model. More strain quantification results are provided for volunteers V10, V14, and V15 for our proposed mesh (red line with plus signs) and the UPF challenger (blue solid line) in Fig. 5 (Right). We averaged the strain curves along the septal wall, where the quality of the myocardium is higher in the acquired images, and the lateral wall, where the myocardium suffers from artifacts due to out-of-region effect and interference with the surrounding structures. As shown in Fig. 5 (Right), strain analysis using the selected deforming mesh usually outputs more similar peak values to the reported measurements by Moore et al. [31] and converges to zero better.

The fourth column in Table 1 summarizes the parameter values that were used for this dataset. We tried to fix the parameter values for all the experiments on both our dataset and the cMac dataset. The value for orientation angle (θ_{int}) for the Gabor filters bank depends on the orientation of the applied tags on the MRI images and is specified for each scanned image sequence. For our dataset and the cMac dataset the orientations were fixed for all

the scanned subjects and were set to $\{-\frac{\pi}{4}, \frac{\pi}{4}\}$ and $\{0, \frac{\pi}{2}\}$, respectively. We used the same λ value, and number of control points specified in the manuscript for the cMac dataset ($\lambda = 0.1$, 4 control points) by Craene et al. [17] The same λ value was used for the experiments on our dataset, but we increased the number of control points to 5 to handle the challenging problem of estimating a 2D displacement field for the 2D tagged MRI sequences from the actual 3D movement of the LV. The number of samples were set to around 15% percent of the total number of voxels for both datasets as suggested by the authors. Different values for the threshold and the standard deviation (σ) were tested for the Gaussian filter for randomly sampled tagged MR images from the two datasets to get images with sufficiently reduced noise and to make sure that the identified super-pixels are not too small. The identified values were fixed for all the subjects in each dataset. γ for the upward ramping function was set to 0.25 for both datasets to slightly enhance the contrast of the combined motion and magnitude response images. All the other parameter values were adjusted to achieve a high accuracy while preventing the proposed algorithm from being very slow. These values were kept fixed for both datasets. This explanation is added to validation section.

5. Discussion

Our algorithm provides full-cycle segmentation for the tagged MRI sequence and excludes papillary muscles from the segmentation. The proposed algorithm considers all the frames in the decision-making process for aligning the cine and tagged MR images. The mean distance error measurement for the proposed algorithm and expertsâ segmentations is less than 2.57 mm for our dataset consisting both healthy cases and patients suffering from degenerative mitral regurgitation (DMR). It is important to point that manual segmentation for tagged MR images is also found to be challenging and the measured inter-observer-variability is on average more than 1.19 mm.

The distance error measurement between the segmented contour by the proposed algorithm by Montillo et al. [3] for tagged MR images and the expert segmentation is less than 3 pixels for LV and RV epicardium for 83% of the cases and less than 3 pixels for LV endocardium for 59% of the cases on tagged MR images with single tag lines and all the frames within the cardiac cycle. Histace et al. [6] propose a segmentation algorithm for tagged MR images with double tag lines (± 45). Their algorithm performs segmentation for frames selected from the systolic phase only and propagates the segmentation to the other frames using motion tracking. Garcia-Barnes et al. [7] perform segmentation for tagged MR images with double tag lines (± 45) for the End-diastolic phase only. Qian et al. [5] perform tagged MRI segmentation for images with single tag orientations: 0, +45, -45, or 90. However, their dataset has higher quality compared to the standard tagged MRI sequences were tags fade in later frames of the cardiac phase. The work by Wang et al. [8] does not perform segmentation for the 1st and 2nd frame of the tagged cardiac cycle where the LV is obscured by strong tag lines and segments the 3rd to the 20th frames for cases consisting 20 frames in the whole cardiac cycles. Metaxas et al. [10] do segmentation for images with vertical single tagging for 7 healthy subjects. All these methods do not take any steps to exclude papillary muscles in the LV segmentation.

Camara et al. [11] propose an algorithm for shift correction between tagged and cine MRI sequences. In this way cine segmentation can be mapped to the tagged MRI sequence. However, unlike our algorithm, the proposed algorithm utilizes the ED frame only for shift correction. Shi et al. [12] de-tag images in three 3D tagged MRI sequences, register the de-tagged 3D MR image sequences to generate a 4D pseudo-anatomical image and finally register the 2D cine images to the 4D pseudo-anatomical image. Similar to

our work, this algorithm considers all the frames while registering the cine and tagged slices and excludes papillary muscles since it maps cine segmentation to the corresponding tagged MRI sequence. However, a 3D tagged image sequence is required to utilize this algorithm and edge information is removed in the de-tagging process which may adversely affect the registration outcome. The distance error measurements between the proposed segmentation and the expert segmentation for these methods, when reported, was in the range of more than 1 pixels and less than 3 pixels.

The spatial resolution of MR images in the previous studies and our study is not consistent. This difference affects the performance outcomes of the proposed algorithm as well as the previously proposed methods. As a result, we provide the mean distance error in millimeters for these algorithms together with the spatial resolution of MR images (where provided) that were used to evaluate the algorithm in the following. In millimeters, Qian et al. [5] report mean Euclidean distance error of less than 2 mm. Camara et al. [11] report mean Euclidean distance error of less 2.04 mm for MR images with spatial resolution of 0.78 mm. The algorithm proposed by Garcia et al. [7] provides a mean Euclidean distance error below 2.48 mm for basal, mid-ventricular, and apical regions for MR images with spatial resolution of 1.24 mm. Shi et al. [12] report median distance error of 1.04 mm for endocardium surface tracking and 0.76 mm for epicardium distance tracking for MR images with spatial resolution of 1 mm.

Previously proposed algorithms for tagged myocardium segmentation depend on either not generally reliable features or at most two out of the three utilized features in this paper, namely, tag patterns, motion, and edge information. Motion is the most reliable and always existing feature which Garcia-Barnes et al. [7] used together with Gabor filter magnitude responses to segment tagged myocardium. Their proposed algorithm, however, suffers from the blurred-boundaries problem. By adding edge information to the proposed method by Garcia-Barnes et al. [7], we were able to robustly identify the myocardium in the whole cardiac cycle with detailed myocardium boundaries.

Analysis is performed for both subjects with 2D tagged MRI sequences using our dataset and subjects with 3D tagged MRI sequences using the cMac dataset. Therefore, the experiments performed on the cMac dataset estimate both the radial and longitudinal motion of the LV and this information is taken into account while combining motion information with the magnitude responses acquired by applying the Gabor filters bank. For the 2D tagged MRI sequence, the estimated motion from the tagged MRI sequence in the cardiac cycle is not an accurate estimation of the longitudinal and radial movement of the LV. One can say that the estimated displacement is a rough 2D approximation of the actual 3D movement that the LV experiences. However, since the cine MRI sequence is scanned from the same LV and from the same planes, both sequences are experiencing approximately the same longitudinal and radial motion. Consequently, the estimated displacement field can be used to register the magnitude responses of tagged images from different time frames to the target frame and use the proposed similarity metric to map cine segmentation of an image slice to the corresponding slice in the tagged MRI sequence.

Ventricular remodeling can happen because of certain cardiac conditions such as myocyte hypertrophy, myocyte apoptosis, myofibroblast proliferation, and interstitial fibrosis. In several studies, such as in the work by Grayburn et al. [36], left ventricular remodeling has been identified in patients with degenerative mitral regurgitation. Under such conditions, the short-axis cut through the left ventricle may not have an exactly circular shape. In our similarity metric, the centricity energy works as a regularization term that tries to center the segmentation on the LV muscles. In other words, like many model-based LV myocardium segmentation algorithms, we assume that LV myocardium in the short-axis view is

almost (but not necessarily exactly) circular. As reported in the validation section, we tested our cine-to-tagged segmentation mapping algorithm on patients suffering from degenerative mitral regurgitation and our results confirm that the proposed algorithm can be used for these patients as well.

Both our dataset and the cMac dataset are acquired using 3T MRI scanners. Although tag fading, lack of visible myocardium borders and blood circulation artefacts are frequently observed in our dataset, it is important to evaluate the proposed algorithm on MRI sequences acquired from 1T and 1.5T scanners to ensure robustness of the proposed algorithm for different types of MRI scanners. Moreover, we used the TDFFD motion tracking algorithm proposed by the UPF challenger in cMac 2011 and compared our results to this challenger's results. Having both used the same motion tracking algorithm with the same parameter values, our results were more similar to the reported strain measurements for healthy hearts in the literature than the UPF challenger's results. One can conclude that the differences result from having a more accurate myocardium segmentation by careful selection of the mesh to propagate to the other phases.

Relying on one specific motion tracking algorithm is a limitation of this work. It is important to see how the registration algorithms proposed by the other challengers in cMac 2011, such as the work by Mansi et al. [32], Knutsson et al. [33], and Shi et al. [34], or the motion tracking methods discussed in [35] perform using the proposed mesh.

6. Conclusion

Myocardial strain analysis is an effective technique for the identification of nonviable myocardium. This analysis requires accurate tracking of the myocardium in tagged MR images as well as correct segmentation of the myocardium during the cardiac cycle. Many algorithms have been proposed for motion tracking for tagged MRI sequences. However, correct segmentation of the myocardium during the cardiac cycle has not been addressed well.

This paper introduces an algorithm to leverage the existing cine MRI segmentation in order to increase accuracy of strain analysis for tagged MR images by ensuring correct full-cycle segmentation of the myocardium. The proposed algorithm incorporates a metric that can effectively locate the myocardium in tagged MRI sequences and can be used to evaluate a proposed full-cycle segmentation for tagged MR images. The proposed metric relies on three different features—tag patterns, motion, and edge information from tagged MR images —and combines them to efficiently differentiate the myocardium from other tissue types. Using the proposed metric to map cine MRI segmentation on tagged MR images and to find the deforming mesh with the most accurate full-cycle myocardium segmentation contributed to more accurate segmentation and regional strain analysis of the left ventricular myocardium in tagged MR images.

Declaration of Competing interest

None.

Supplementary material

Supplementary material associated with this article can be found, in the online version, at doi:10.1016/j.cmpb.2019.105128.

References

[1] O. Smiseth, H. Torp, A. Opdahl, K. Haugaa, S. Urheim, Myocardial strain imaging: how useful is it in clinical decision making? Eur. Heart J. 37 (15) (2015) 1196–1207, doi:10.1093/eurheartj/ehv529.

[2] P. Morais, B. Heyde, D. Barbosa, S. Queiros, P. Claus, J. D'hooge, Cardiac motion and deformation estimation from tagged MRI sequences using a temporal coherent image registration framework, in: International Conference on Functional Imaging and Modeling of the Heart, 2013, pp. 316–324, doi:10.1007/978-3-642-38899-6_38.

[3] A. Montillo, D. Metaxas, L. Axel, Automated segmentation of the left and right ventricles in 4D cardiac SPAMM images, in: Medical Image Processing and Computer Assisted Intervention, 2002, pp. 620–633, doi:10.1007/3-540-45786-0_77.

[4] J. Milles, A. van Susteren, T. Arts, P. Clarysse, P. Croisille, I. Magnin, Automatic 2D segmentation of the left ventricle in tagged cardiac MRI using motion information, in: IEEE International Symposium on Biomedical Imaging: Nano to Macro, 1, 2004, pp. 153–156, doi:10.1109/ISBI.2004.1398497.

[5] Z. Qian, D. Metaxas, L. Axel, A learning framework for the automatic and accurate segmentation of cardiac tagged MRI images, in: International Workshop on Computer Vision for Biomedical Image Applications, 2005, pp. 93–102, doi:10.1007/11569541_11.

[6] A. Histace, B. Matuszewski, Y. Zhang, Segmentation of myocardial boundaries in tagged cardiac MRI using active contours: a gradient-based approach integrating texture analysis, J. Biomed. Imaging 4 (2009), doi:10.1155/2009/983794.

[7] J. Garcia-Barnes, A. Andaluz, F. Carreras, D. Gil, Decoupled external forces in a predictor-corrector segmentation scheme for LV contours in tagged mr images, IEEE Eng. Med. Biol. Soc. (2010) 4805–4808, doi:10.1109/IEMBS.2010.5628029.

[8] Z. Yu, Q. Wang, W. Xiong, Z. Yu, C. Zhang, H. Hu, Segmentation of cardiac tagged MR images using a snake model based on hybrid gradient vector flow, Multimed. Tools Appl. (2017) 1–26, doi:10.1007/s11042-017-5013-2.

[9] T. Denney, B. Gerber, L. Yan, Unsupervised reconstruction of a three-dimensional left ventricular strain from parallel tagged cardiac images, Magn. Reson. Med. 49 (4) (2003) 743–754, doi:10.1002/mrm.10434.

[10] D. Metaxas, L. Axel, Z. Qian, X. Huang, A segmentation and tracking system for 4D cardiac tagged MR images, IEEE Eng. Med. Biol. Soc. (2006) 1541–1544, doi:10.1109/IEMBS.2006.259652.

[11] O. Camara, E. Oubel, G. Piella, S. Balocco, M.D. Craene, A. Frangi, Multi-sequence registration of cine, tagged and delay-enhancement MRI with shift correction and steerable pyramid-based detagging, in: Functional Imaging and Modeling of the Heart, 2009, pp. 330–338, doi:10.1007/978-3-642-01932-6_36.

[12] W. Shi, X. Zhuang, H. Wang, S. Duckett, D. Luong, C. Tobon-Gomez, K. Tung, P. Edwards, K. Rhode, R. Razavi, S. Ourselin, A comprehensive cardiac motion estimation framework using both untagged and 3-D tagged mr images based on nonrigid registration, IEEE Trans. Med. Imaging 31 (6) (2012) 1263–1275, doi:10.1109/TMI.2012.2188104.

[13] A. Makram, M. Rushdi, A. Khalifa, M. El-Wakad, Tag removal in cardiac tagged MRI images using coupled dictionary learning, IEEE Eng. Med. Biol. Soc. (2015) 7921–7924, doi:10.1109/EMBC.2015.7320229.

[14] D. Peters, D. Ennis, E. McVeigh, High resolution MRI of cardiac function with projection reconstruction and steady state free precession, Magn. Reson. Med. 48 (1) (2002) 82–88, doi:10.1002/mrm.10193.

[15] T. Chen, X. Wang, S. Chung, D. Metaxas, L. Axel, Automated 3D motion tracking using Gabor filter bank, robust point matching, and deformable models, IEEE Trans. Med. Imaging 29 (1) (2010) 1–11, doi:10.1109/TMI.2009.2021041.

[16] M. Li, H. Gupta, S. Lloyd, J.T.D. Dellaltalia L. and, A graph theoretic approach for computing 3D+ time biventricular cardiac strain from tagged MRI data, Med. Image Anal. 35 (2017) 46–57, doi:10.1016/j.media.2016.06.006.

[17] M.D. Craene, C. Tobon-Gomez, C. Butakoff, N. Duchateau, G. Piella, K. Rhode, A. Frangi, Temporal diffeomorphic free form deformation (TDFFD) applied to motion and deformation quantification of tagged MRI sequences, in: International Workshop on Statistical Atlases and Computational Models of the Heart, 2011, pp. 68–77, doi:10.1007/978-3-642-28326-0_7.

[18] C. Tobon-Gomez, M.D. Craene, K. Mcleod, L. Tautz, W. Shi, A. Hennemuth, A. Prakosa, H. Wang, G. Carr-White, S. Kapetanakis, A. Lutz, Benchmarking framework for myocardial tracking and deformation algorithms: an open access database, Med. Image Anal. 17 (6) (2013) 632–648, doi:10.1016/j.media.2013.03.008.

[19] P. Felzenszwalb, D. Huttenlocher, Efficient graph-based image segmentation, Int. J. Comput. Vis. 59 (2) (2004) 167–181, doi:10.1023/B:VISI.0000022288.19776.77.

[20] M. Cheng, N. Mitra, X. Huang, P. Torr, S. Hu, Global contrast based salient region detection, IEEE Trans. Pattern Anal. Mach.Intell. 37 (3) (2015) 569–582, doi:10.1109/TPAMI.2014.2345401.

[21] H. Fadil, J. Totman, S. Marchesseau, 4D automatic centre detection of the right and left ventricles from cine short-axis MRI, in: International Workshop on Statistical Atlases and Computational Models of the Heart, 2016, pp. 143–151, doi:10.1007/978-3-319-52718-5_16.

[22] B. Villard, E. Zacur, E.D. Armellina, V. Grau, Correction of slice misalignment in multi-breath-hold cardiac MRI scans, in: International Workshop on Statistical Atlases and Computational Models of the Heart, 2016, pp. 30–38, doi:10.1007/978-3-319-52718-5_4.

[23] J. Tufvesson, E. Hedstram, K. Steding-Ehrenborg, M. Carlsson, H. Arheden, E. Heiberg, Validation and development of a new automatic algorithm for time-resolved segmentation of the left ventricle in magnetic resonance imaging, BioMed Res. Int. (2015), doi:10.1155/2015/970357.

[24] E. Heiberg, J. Sjagren, M. Ugander, M. Carlsson, H. Engblom, H. Arheden, Design and validation of segment - a freely available software for cardiovascular image analysis, BMC Med. Imaging 10 (1) (2010), doi:10.1186/1471-2342-10-1.

[25] B. Yeo, M. Sabuncu, T. Vercauteren, N. Ayache, B. Fischl, P. Golland, Spherical demons: fast diffeomorphic landmark-free surface registration, IEEE Trans. Med. Imaging 29 (3) (2010) 650–668, doi:10.1109/TMI.2009.2030797.

[26] J. Pluim, J. Maintz, M. Viergever, Mutual-information-based registration of medical images: a survey, IEEE Trans. Med. Imaging 22 (8) (2003) 986–1004, doi:10.1109/TMI.2003.815867.

[27] Y. Peng, A. Ganesh, J. Wright, W. Xu, Y. Ma, Rasl: robust alignment by sparse and low-rank decomposition for linearly correlated images, IEEE Trans. Pattern Anal. Mach.Intell. 34 (11) (2012) 2233–2246, doi:10.1109/TPAMI.2011.282.

[28] R. Szeliski, J. Coughlan, Spline-based image registration, Int. J. Comput. Vis. 22 (3) (1997) 199–218, doi:10.1023/A:100799633.

[29] L. Dice, Measures of the amount of ecologic association between species, Ecology 26 (3) (1945) 297–302, doi:10.2307/1932409.

[30] J. Sternby, Frame deformation energy matching of on-line handwritten characters, in: Iberoamerican Congress on Pattern Recognition, 2005, pp. 128–137, doi:10.1007/11578079_14.

[31] C. Moore, C. Lugo-Olivieri, E. McVeigh, E. Zerhouni, Three-dimensional systolic strain patterns in the normal human left ventricle: characterization with tagged MR imaging, Radiology 214 (2) (2000) 453–466, doi:10.1148/radiology.214.2.r00fe17453.

[32] T. Mansi, X. Pennec, M. Sermesant, H. Delingette, N. Ayache, Ilogdemons: a demons-based registration algorithm for tracking incompressible elastic biological tissues, Int. J. Comput. Vis. 92 (1) (2011) 92–111, doi:10.1007/s11263-010-0405-z.

[33] H. Knutsson, M. Andersson, Morphons: segmentation using elastic canvas and paint on priors, in: IEEE International Conference on Image Processing, 2, 2005, pp. 1226–1229, doi:10.1109/ICIP.2005.1530283.

[34] W. Shi, X. Zhuang, H. Wang, S. Duckett, D. Luong, C. Tobon-Gomez, K. Tung, P. Edwards, K. Rhode, R. Razavi, S. Ourselin, A comprehensive cardiac motion estimation framework using both untagged and 3-d tagged mr images based on nonrigid registration, IEEE Trans. Med. Imaging 31 (6) (2012) 1263–1275, doi:10.1109/TMI.2012.2188104.

[35] J. Woo, M. Stone, Y. Suo, E. Murano, J. Prince, Tissue-point motion tracking in the tongue from cine MRI and tagged MRI, J. Speech Lang. Hear. Res. 57 (2) (2014) S626–S636, doi:10.1044/2014_JSLHR-S-12-0208.

[36] P.A. Grayburn, E. Foster, C. Sangli, N.J. Weissman, J. Massaro, D.G. Glower, T. Feldman, L. Mauri, Relationship between the magnitude of reduction in mitral regurgitation severity and left ventricular and left atrial reverse remodeling after MitraClip therapy, Circulation 128(15) (2013) 1667–1674. 10.1161/CIRCULATIONAHA.112.001039.